CORPUS PUBLISHERS

Current Trends in Engineering Science (CTES)

ISSN: 2833-356X

Volume 3 Issue 6, 2023

Article Information

Received date : September 22, 2023

Published date: October 18, 2023

*Corresponding author

André Cruz da Costa Maciel, Institute of Technology, Federal University of Pará, Guamá, Belém, Pará, Brazil

DOI: 10.54026/CTES/1047

Keywords

Cutting temperature; Sn-Sb alloys; Microstructures; Solidification Thermal Parameter

Research article

Influence of Solidification Parameters and Solute Content on the Machinability of Two Lead-Free Babbit Metals

André Cruz da Costa Maciel[1*], Nádia Silva Cosmo[1], Hércicles Ruiliman Oliveira de Souza[1], Sanderson Dias Maués[1], Ariadne Cristine Botelho Farias[1], Angela de Jesus Vasconcelos[1], Otávio Fernandes Lima da Rocha[2] and Maria Adrina Paixão de Souza da Silva[1]

[1]Institute of Technology, Federal University of Pará, Guamá, Belém, Pará, Brazil

[2]Federal Institute of Pará, Marco, Belém, Pará, Brazil

Abstract

Studies suggest that white metal Sn-Sb alloys are the most commonly type of babbit metal used in industry. However, it is necessary to evaluate manufacturing characteristics and solute contents that leads the best machining conditions. This work presents a correlation between solidification parameters and machinability of Sn-2.0wt%Sb and Sn-5.5wt%Sb alloys, solidified in a horizontal directional device, evaluating the influence of solute content on these results. Cutting temperatures were measured in dry necking processes along the length of the ingot. It was observed that the reverse cellular-dendritic transition influenced the cutting temperature results. The range of cell and dendrite spacings varies approximately from 40 to 330 µm on the Sn-2.0wt%Sb alloy and from 15 to 240 µm on the Sn-5,5wt%Sb alloy. In the cellular region, higher values are found for the Sn-5.5wt%Sb alloy, but in the dendritic region, these values were higher for the Sn-2.0wt%Sb alloy.

Introduction

Alloys containing tin, antimony, copper, and lead are recommended for a variety of applications due to their excellent friction behavior, reasonably good corrosion resistance, and low cost. These alloys, known as Babbitt or White metal, combine good load-carrying capacity, low wear, good running-in behavior, and work well in emergencies, such as the absence of adequate lubrication [1,2].

Among this set of alloys, tin-based alloys such as those in the Sn-S-b system, are the most commonly used because of their characteristics, such as good corrosion resistance, ease of bonding, low tendency towards segregation, and high thermal conductivity [3-5]. In addition, tin-based alloys also have better wear resistance, tensile strength, and fatigue resistance, which makes them useful in applications that require high strength and durability [6]. They also have good welding properties, which facilitate their application in manufacturing processes [7,8], and do not constitute a hazardous substance, such as lead alloys, which are prohibited by the EU's Restriction of Hazardous Substances (RoHS) [7-10]. The Sn-Sb alloys are commonly used as patent metal in various applications, such as in the manufacture of batteries, electronic equipment, automotive parts, and kitchen utensils, among others [4,6]. In batteries, for example, Sn-S-b alloys are used as grid material for electrode manufacturing, due to their high corrosion resistance and good electrical conductivity [11-13].

The structure of Sn-Sb alloys represents a soft α-Sn matrix with reinforcing particles of SnSb intermetallic compounds (IMCs) [12]. One of the interesting studies to be carried out for these alloys is related to their solidification process since it is known that controlling the variables of this process, such as growth (VL) and cooling rate (TR), affects the microstructural development of these alloys, dendritic growth, distribution and morphology of their intermetallic compounds, making it possible to guarantee the final product mechanical and manufacturing characteristics arising from the microstructure formed, since all are interrelated [12-14].

In all these applications, during the manufacturing process of the components, they will be machined at least once. In this way, the study of the characteristics that result in better behavior of the material during the machining process (machinability) is of fundamental importance [15-19], although, due to several variables involved in the processing of materials, it is not possible to establish a single process or condition that results in better machinability. In this sense, the formation of a database with experimental results under different conditions reduces the risk of errors during the processing of the material. It is known that the work performed in the metal machining process is converted into heat because of the existing friction forces and will depend on the material to be machined (including solute content). Ductility, hardness, and thermal properties have a significant effect on the acting forces and the generated temperature. Thus, there is great importance in measuring temperatures during machining operations and in studying their effects, as one of the machinability criteria [18-21].

As said, the variables of the solidification process and the resulting structures can significantly influence the machinability of materials, and recent studies have confirmed that evaluating the solidification process as an initial step in verifying the ease or difficulty of machining a material can guarantee not only improvements in the final state of the part and cheaper costs [18,19,22,23], but even though the use of this information in the industrial manufacturing processes of parts produced with Sn-Sb alloys can avoid unnecessary expenses resulting in the best mechanical benefit of the manufactured material, including the limitations of toxicity, were not found analyzes that relate solidification thermal parameters and structural characteristics with machinability in this alloy system.

In this sense, this work aims to make a correlation between solidification parameters (i.e., growth and cooling rates and primary dendrite arm spacings) and machinability of hypoperitectic Sn-2.0wt%Sb and near peritectic Sn-5.5wt%Sb alloys, solidified in a horizontal directional device, by cutting temperature criteria, evaluating the influence of solute content on these results.

Material and Methods

Experiments of horizontal directional solidification were performed with Sn–xSb (x=2.0wt% by Rocha (2018) and 5.5wt%) alloys, which corresponding phase diagram is presented in figure 1. The chemical compositions of metals used to prepare these alloys are given in table 1.

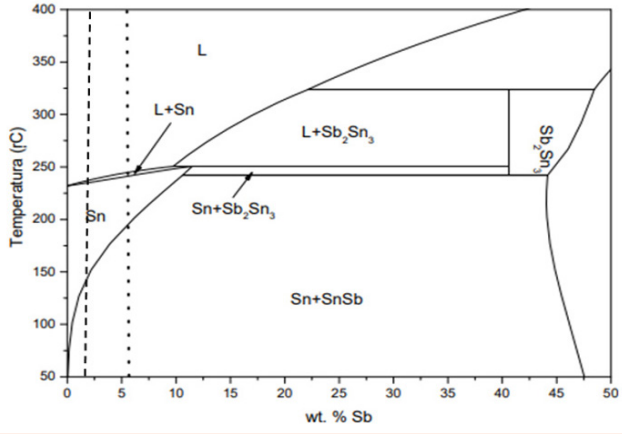

Figure 1: Sn-Sb phase diagram of Rocha (2018).

Table 1: Chemical composition of metals used to prepare alloys (mass fraction, %) [19].

Element	Pb	Fe	Cd	Ni	Cu
Sn	0.0469	0.0081	0.00001	0.00001	0.0047
Sb	0.215	0.075	-	0.034	0.034
Element	Bi	Zn	Si	Sb	Sn
Sn	0.0046	0.0001	-	0.0005	Bal.
Sb	-	-	0.009	Bal.	-

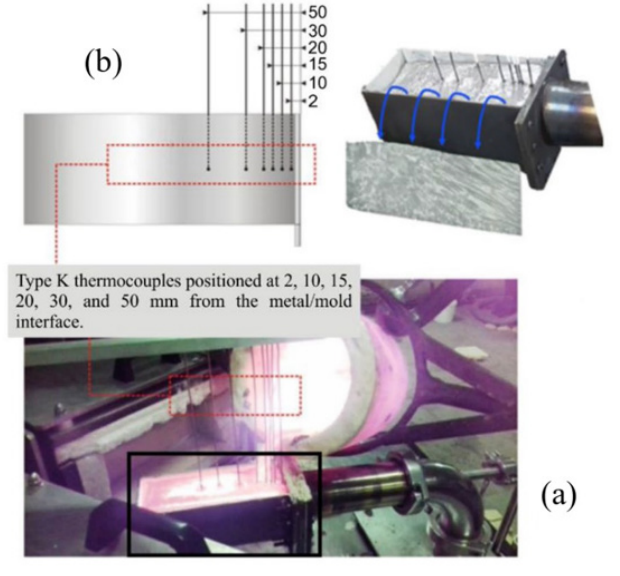

Figure 2: Experimental representation of the horizontal solidification device of the investigated alloy: (a) pouring and (b) positions of the thermocouples de Azevedo (2020).

The alloys were solidified in a horizontal directional solidification device (HDS), designed in such a way that the heat of the metallic liquid was extracted only through a water-cooled system on one of the side walls of the mold, thus promoting horizontal solidification. Figure 2 presents a photographic record during liquid metal pouring into the rectangular ingot mold installed inside the water-cooled horizontal directional solidification device, as well as details of mounting the thermocouples inside the mold at positions from the cooled interface. The stainless-steel mold used has a wall thickness of 3mm, a length of 160mm, a height of 60mm and a width of 60mm. More details on horizontal solidification device can be found in recently published works [24-26]. The thermocouples were used to monitor temperatures along the length of the casting and these data were acquired automatically. With temperature profile results, growth rate (v_L) and cooling rate (T_R) could be obtained for the investigated alloys, according to the methodology of reference of Costa et al. [18].

After the complete solidification of the alloys, the as-cast ingots were sheared along its longitudinal direction and prepared using metallographic techniques, following the evaluation of the directionality of the heat extraction, and identifying the limit of formation of the grains, which were presented in two distinct regions: columnar and columnar-to-equiaxed transition. For the microstructural characterization, cuts were made along the ingot to get and quantify the primary dendritic arm spacing (λ_1). Metallographic procedures followed the cuts to reveal and visualize the microstructure, with etching using acid solution of 1 ml of HF, 2 ml of HCl, 3 ml of HNO_3, and a mixture of H_2O and ethyl alcohol to achieve 100 ml. The determination of the length scale of the microstructure along the length of the HDS castings was performed through micrographs acquired using a Metallurgical Microscope and due to the difficulty of observing dendrite cores, two different methods were used to measure primary dendritic spacing: the triangle method of Rocha [27] and the line intersection method of Oliveira et al. [28] & Çadirli et al. [29].

Necking is not usual for machining operations, but as there was no turning process to change the geometry of the cross section from rectangular to circular to avoid recrystallization and modification of the ingot macrostructure, the depth of the penetration adopted was the whole dimension of the section, characterizing necking process. Nevertheless, necking is a usual kind of machinability test [30]. Then, given the chief aim of correlating machinability, solute content, and solidification aspects of Sn-2.0wt%Sb and Sn-5.5wt%Sb alloys, such as λ_1, the dry necking process was carried out in the longitudinal section of the ingots. The experiment was carried out in a semiautomatic bench lathe, and conventional HSS T6 ¾" high-speed steel chisels were used as a cutting tool, with their original polishing and sharpening (Figure 3). The choice of conventional lathe is because of still wide application in an industrial scale [19,21] and the choice of tool material is because of its low cost combined with good hot hardness, which makes this tool material also widely used in industry. The dimensions of the specimens and the rotations were established in such a way that the average cutting speed was parameterized around 40 m/min, for an advance of 0.1 mm/rev and, in this way, the neckings were performed in the following positions: 0-10, 11-20, 21-30, 31-40, 41-60, and 61-80 mm along the casting length.

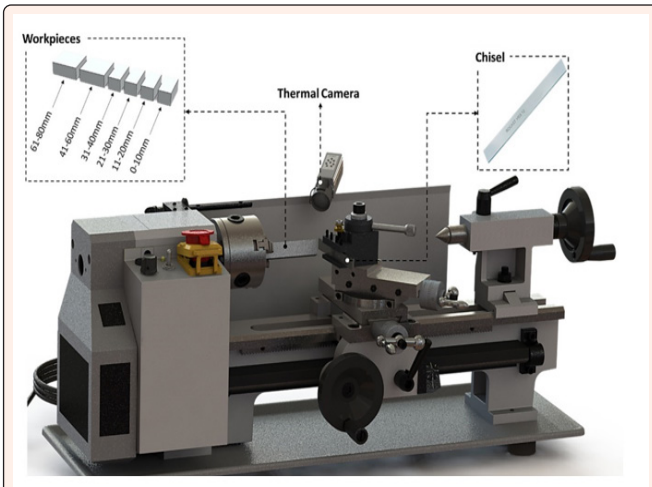

Figure 3: Schematic representation of the bench lathe showing the necking positions, the thermal camera and the high-speed steel chisels.

For cutting temperature measurement, a digital infrared thermometer was used, and a measurement technique already established in the literature [31,32] coupled to a computer running data acquisition software was applied. The thermometer was always directed to the cutting area (Figure 3). More details can be also seen in previous works [18,20,33,34]. With these values, it was possible to obtain the machining heating rates (MHR) for each necking, which is the ratio of the difference between the maximum temperature reached and the initial temperature and the difference between the corresponding times in these temperatures [19,33]. The calculation of the rate is necessary to parametrize the results, since, as the emissivity value of the alloy is not known, the emissivity of the black body is used, so the temperatures got directly from the infrared thermometer are relative values.

Results

Solidification kinetics and microstructure

Figure 4 shows the experimental cooling curves furnished by the thermocouples at different positions (P) in the centerline of the HDS castings concerning the cooled side of the casting (P = 0), for the Al-2.0wt%Sb alloy of Rocha et al. [27] and Sn-5,5wt%Sb alloy. The horizontal lines show the experimentally determined liquidus temperature of each examined alloy.

By using the temperature results of the cooling curves, and the procedures stated in Costa et al. [18], position as a function of the time of the liquidus slope passing by each thermocouple is presented, also in figure 4.

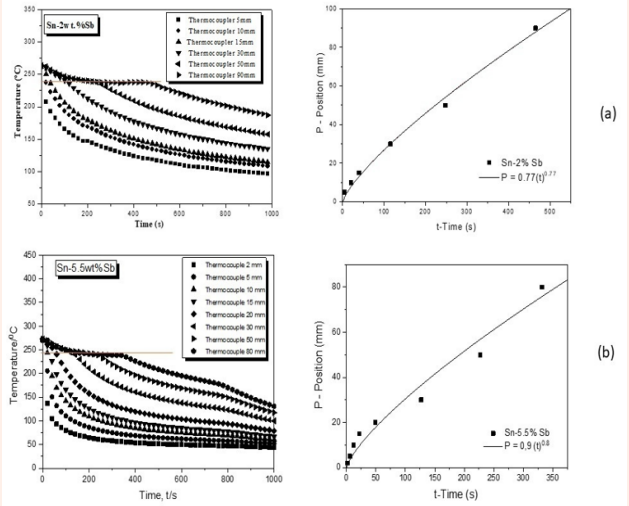

Figure 4: Experimental cooling curves and experimental time corresponding to the passage of liquid isotherm by each thermocouple position for the Sn-xSb alloys: (a) x=2wt.% of Rocha (2018) and (b) x=5.5wt.%.

The experimental thermal data from figure 4 was used to determine the growth and cooling rates (VL and TR) for each Sb composition, and the results are shown in figure 5. As expected, the water-cooled horizontal solidification system imposed for high VL and TR near the heat transfer surface (cooled mold plate), which decrease as the solidification layer grows along the longitudinal length, obviously due to the thermal resistance of heat transfer by conduction.

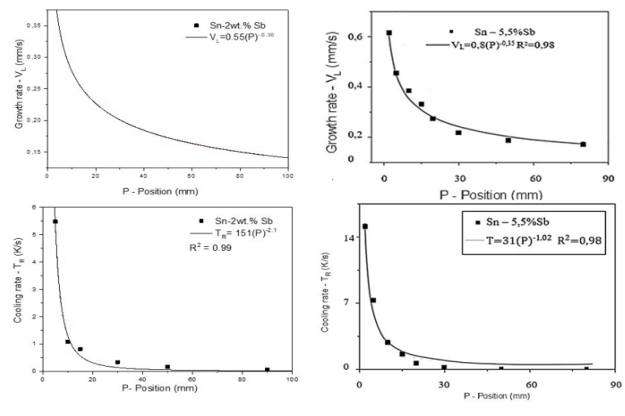

Figure 5: Growth and cooling rates as a function of position for the Sn-xSb: (a) x=2wt.% of Rocha (2018), and (b) x=5wt.% alloys.

The microstructure of both compositions has been characterized by a Sn-rich matrix of either cellular or dendritic morphologies, as shown in figure 6. During the horizontal solidification, the microstructure exhibits a cellular/dendritic reverse transition, i.e., the microstructure has a cellular morphology for a region close to the cooled mold, changing to a dendritic morphology with the decrease in cooling rate and growth rate along a transition zone. These cells are called high-growth rate cells in the literature of Trivedi et al. [34] however, in their study, Rocha et al. [27] proposed that under transient solidification conditions, high-cooling rate cells seem to be a more appropriate designation since both the growth rate and the thermal gradient (GL) vary continuously, are interdependent and can be combined by the cooling rate (TR=GL·VL). This type of morphology can be considered atypical and very rare in metallic alloys [14,34,36].

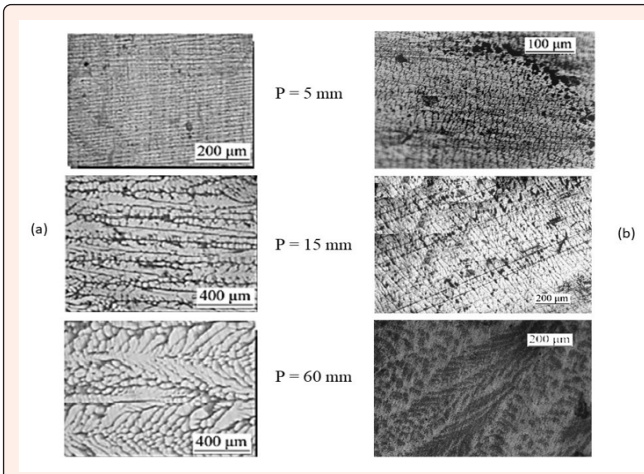

Figure 6: Microstructures for the analyzed alloys: (a) Sn-2.0wt%Sb19 and (b) Sn-5.5wt%Sb.

The difference between the two solute contents is that higher cooling and growth rates were obtained for the Sn-5.5wt%Sb alloy, which resulted in a more refined microstructure.

Machinability

Figure 7 (a) & (b) show the results of relative cutting temperatures (according to the emissivity used, of the black body) as a function of the experiment time for each of the analyzed alloys. An increase in temperature is verified in all neckings, followed by a decrease at the end of the process, with the establishment of a regime at the beginning of each test. It is also noticed that during the temperature acquisition, small oscillations appeared in the experimental signal, even after the noise treatment, but that can be attributed to the acquisition system and/or to external factors.

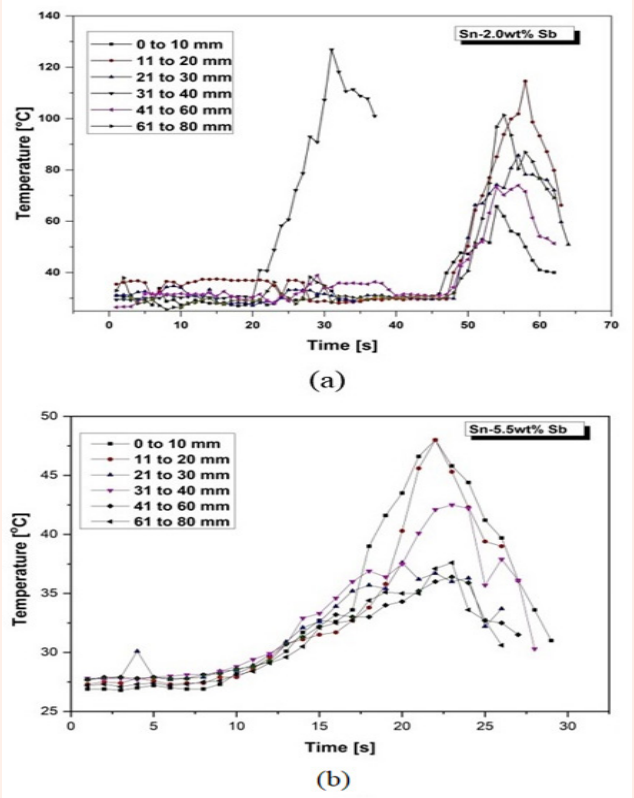

Figure 7: Temperature versus time for the neckings performed along the casting length, for (a) Sn-2.0wt%Sb and (b) Sn-5.5wt%Sb alloys.

A different behavior was verified in the fourth experiment of the Sn-2.0wt%Sb alloy (Figure 7 (a)), with values of maximum cutting temperature higher than the other neckings and anticipation of the maximum cutting temperature. This is because of the breakage of this tool during this necking, which made it impossible to compare this necking with the others.

At the time of increase and decrease of each necking, the temperature variation curves follow the behavior observed in the literature, with an increase to a maximum point followed by a decline at the end of the process [19,37]. As for the establishment of a regime at the beginning of each process, this may be because of the geometry variation (non-circular cross-section) at the beginning of the process, which probably manifests itself more clearly in some alloy systems, such as the case of this work.

Manipulating Stefan-Boltzmann equation, the actual cut-off temperature can be got by isolating the actual temperature in the radiation energy conversion equation, i.e.,

$$T_R = T_{ap} \cdot \sqrt[4]{\frac{\varepsilon_{ap}}{\varepsilon_R}} \qquad (eq.\ 1)$$

where TR is the real temperature, Tap is the apparent temperature, shown by the thermographic sensor, εap is the apparent emissivity (in the case of the black body, 0.95 – the highest existing emissivity value) and εR is the real emissivity of the alloy.

Specific measurement methods must be used to calculate the real emissivity of the alloy; however, it is observed that the real temperature will be higher than the temperatures presented in the results. To verify the maximum temperature obtained in the experiments, the emissivity of the element with the highest mass composition present in the alloy was used, in this case, tin (0.07) [38]. The maximum temperatures for each necking, for each alloy (excluding the fourth neckings for the Sn-2.0wt%Sb alloy), are found in Tables 2 & 3, which presents the temperatures obtained after the energy conversion and the comparison with the alloy recrystallization temperature, around 152 and 193.5oC for the Sn-2.0wt%Sb and Sn-5.5wt%Sb alloys, respectively.

Table 2: Comparison between the values of the maximum cutting temperature obtained in each necking with the sensor, after the conversion, and with the recrystallization temperature of the Sn-5.5wt%Sb alloy.

Recrystallization Temperature (°C)	Position (mm)	Tap (°C)	TR (°C)	Comparison
152	0 to 10	65.7	126.1	Smaller
152	11 to 20	114.6	219.9	Bigger
152	21 to 30	85.7	164.5	Bigger
152	31 to 40	-	-	-
152	41 to 60	73.9	141.9	Smaller
152	61 to 80	111.3	213.6	Bigger

Table 3: Comparison between the values of the maximum cutting temperature obtained in each necking with the sensor, after the conversion, and with the recrystallization temperature of the Sn-5.5wt%Sb alloy.

Recrystallization Temperature (°C)	Position (mm)	Tap (°C)	TR (°C)	Comparison
193.5	0 to 10	48	92.1	Smaller
193.5	11 to 20	48	92.1	Smaller
193.5	21 to 30	36.7	70.4	Smaller
193.5	31 to 40	42.5	81.6	Smaller
193.5	41 to 60	36.4	69.9	Smaller
193.5	61 to 80	37.6	72.2	Smaller

Based on the table, the alloy recrystallization temperature was reached in three neckings, only for the Sn-2.0wt%Sb alloy: in the second, third, and sixth neckings.

Observing the results of the Sn-2.0wt%Sb alloy, it is verified that there is a reverse microstructural transition at the beginning of the ingot, with the occurrence of finer dendritic microstructure in positions closer to the base of the ingot and coarser for more distant positions. The same reverse transition is observed for the Sn-5.5wt%Sb alloy. These morphological changes may be a probable justification for the results found: the cutting temperature is lower in a region of cellular microstructure, increases in the region of dendritic microstructure, but decreases with increasing spacing between the dendritic arms. The last point for the results of Sn-2.0wt%Sb alloy may be probably result of a macrostructural transition. Silva et al. [21] & Silva et al. [33], in their machinability studies in Al-Si and Al-Cu alloys, respectively, also found variations in the cutting temperature with the change in the solidification macrostructure.

Figures 8 & 9 show the machining heating rate as a function of position from the cooled mold interface for both alloys. Here, the influence of the solidification and microstructure are emphasized, as previously discussed. As the neckings, for parameterization reasons, were made in specific positions of the ingot, it was only possible to establish experimental laws that represent the correlations between machining heating rate and position from the metal/mold interface or solidification thermal/structural parameters. It is observed that, for the Sn-2.0wt%Sb alloy, in

the dendritic microstructure region, the machining heating rate decreases with the increase from the metal/mold interface. As for the Sn-5.5wt%Sb alloy, the machining heating rate is relatively constant in the dendritic microstructure region and also appears to have a constant behavior in the cellular microstructure region, with the latter having around twice the value from the first.

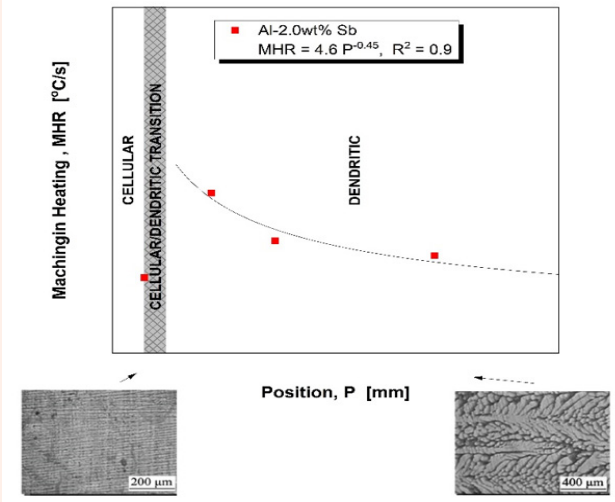

Figure 8: Machining Heating Rate as a function of position from metal/mold interface, for the Sn-2.0wt%Sb alloy.

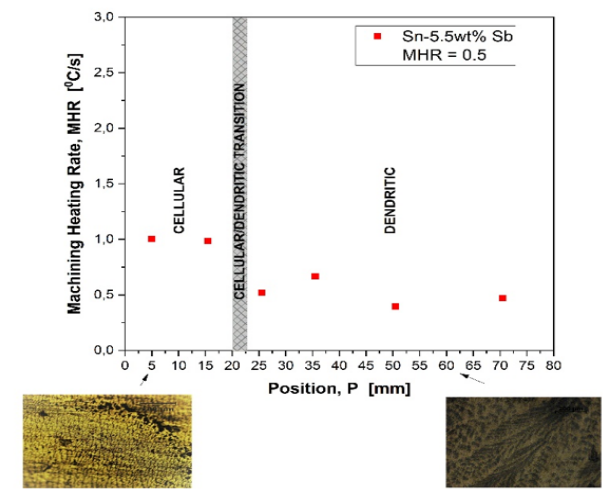

Figure 9: Machining Heating Rate as a function of position from metal/mold interface, for the Sn-5.5wt%Sb alloy.

Figure 10 (a), (b) & (c) shows the results of machining heating rate as a function of growth rate, cooling rate, and primary dendritic spacing in the dendritic microstructure region for the two studied alloys. It is verified that, for the Sn-2.0wt%Sb alloy, the machining heating rate increases with the increase of vL and TR and decreases with the increase of λ1, while for the Sn-5.5wt%Sb alloy the values remain constant throughout the entire ingot.

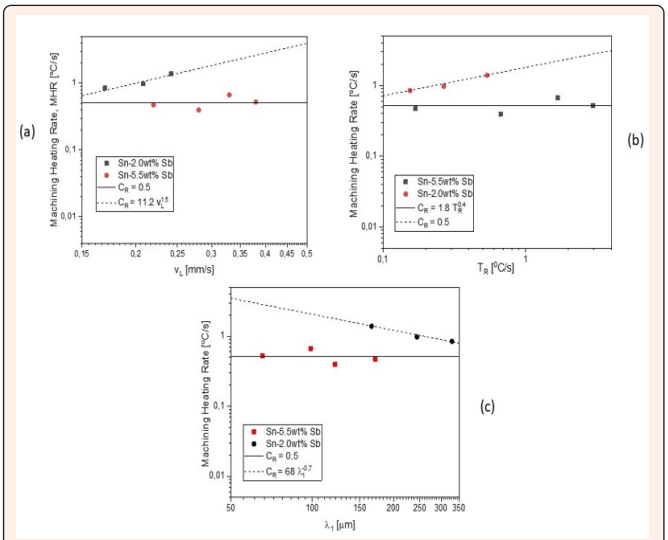

Figure 10: Comparative results of Machining Heating Rate as a function of (a) growth rate, (b) cooling rate and (c) primary dendrite arm spacings for Sn-2.0wt%Sb and Sn-5.5wt%Sb alloys.

It is known that the microstructure of alloys of a peritectic system solidified out of equilibrium comprises dendrites of a primary phase in a matrix of a second phase [14]. For the Sn-Sb alloy system, there is a dendritic region formed by the β-Sn solid solution and, in the dendritic interstices, particles of the SnSb phase [14,39]. The closer to the peritectic composition, the greater the amount of the SnSb phase will be present in the alloy. Finer β-Sn cells have been associated with higher tensile strength, which has been accredited to homogeneously distributed SbSn intermetallic particles (IMC) throughout the intercellular regions [39]. Studies also show that the increase in cutting temperature is related to existing efforts in the machining process or even to the melting of the material to be machined [37,40].

The combination of these factors can be the justification for the results found for the comparison between the solute content of the alloys: an alloy farther from the peritectic composition (Sn-2.0wt%Sb) has a greater amount of solid solution. The solid solution in question, rich in tin, has a low melting point. Here, it is assumed that the temperatures generated during the cutting process handle the melting or softening of solid solution during the necking process, which justifies the higher values of the cutting rates found. In this case, neither a more refined microstructure nor even a greater amount of hard particles (SnSb) generated enough cutting efforts for the machining heating rates of the Sn-5.5wt%Sb alloy to be higher than those of the Sn-2.0wt %Sb. The softening or melting of the material during the cutting process leads to the formation of a false edge, which, depending on the amount, takes on the cutting function, impairing the finish of the piece [41-44].

When analyzing the alloys separately, it is noticed that both the dendritic microstructure and the quantity, size, and distribution of the particles of the SnSb phase directly influence the results: For the Sn-2.0wt%Sb alloy, refined dendritic spacing and homogeneously distributed of SnSb phase (a consequence of higher cooling rates) leads to higher machining heating rates; for the Sn-5.5wt%Sb alloy, the refined microstructure obtained for high cooling rates, which normally generates greater cutting efforts, has the same weight as the quantity and size of the hard SnSb particles, resulting in similar behavior in the Sn-5.5wt%Sb alloy for the cutting temperatures in the necking process.

A machinability analysis only by one criterion is not a factor to guarantee that one condition is better than the other, since the behavior of tool wear, roughness, chip shape, etc., can vary with the number of macro and microstructural variables

that are obtained during the solidification process, however, they can already predict a possible behavior of the material during the machining process under the established conditions and cutting parameters, serving as an aid when choosing the alloy contents and solidification parameters that lead to the best results.

Conclusion

From all the results got, it can be concluded that:

a) Sn-Sb alloys still make up an intriguing system to be considered, since slight variations (composition, mode of heat inheritance, etc.) can significantly affect their morphology and their performance in the manufacturing process.

b) The results of the Sn-2.0wt%Sb alloy show that microstructural transition interferes with the cutting temperatures, as well as dendrite arm spacing, with a decreasing profile with distance from metal/mold interface-increase of λ1 on this last one. The amount of β-Sn phase of the alloy also contributed to the machining heating rates obtained. The high cutting temperatures got in refined dendritic structures and on CET also led to reaching the alloy recrystallization temperature. Power function laws could represent the behavior of machining heating rates as a function of position, solidification thermal parameters, and primary dendrite arm spacing, on the dendritic region.

c) The results of the Sn-5.5wt%Sb alloy also indicate that microstructural transition interferes with the cutting temperatures, with machining heating rates constant in the dendritic microstructure region and appears to have a constant behavior in the cellular microstructure region, with the latter having around twice the value from the first. The refined microstructure obtained has the same weight on the machining heating rate as the quantity and size of the hard SnSb particles resulting from this constant profile.

d) Based on cutting temperature criteria, even though the Sn-5.5wt%Sb alloy has greater mechanical resistance than the Sn-2.0wt%Sb alloy, when presenting a dendritic microstructure, it has lower cutting temperatures, for the parameters established in this work, regardless of the thermal solidification parameters.

Acknowledgment

The authors acknowledge CNPQ for funding this research and to the Federal Instuitute of Pará (IFPA) for the technical and scientific support for this study.

References

1. Kamal M, El Bediwi A, Lashin A, El Zarka A (2011) Copper effects in mechanical properties of rapidly solidified Sn-Pb-Sb Babbitt bearing alloys. Materials Science and Engineering A 530(1): 327-332.
2. Ribeiro R, Câmara M (2020) Study of the tribological behavior of the Babbitt alloy pair - ABNT 1045 steel when varying the thickness and roughness of the coating. Article 25(2).
3. Lashin A, Mossa M, El-Bediwi A, Kamal M (2013) Study of some physical properties of the rapidly solidified Sn-Sb-Cu-Zn alloys. Materials and Design 43: 322-326.
4. Valeeva A, Valeev I, Fazlyakhmetov R (2017) Microstructure of the β -Phase in the Sn11Sb5.5Cu Babbit. Physics of Metals and Metallography 118(1): 48–51.
5. Zeren A (2007) Embeddability behaviour of tin-based bearing material in dry sliding. Materials and Design 28(8): 2344-2350.
6. Lashin A, Mossa M, Kamal M (2011) Indentation creep and mechanical properties of quaternary Sn – Sb based alloys. Materials Science & Engineering A 528: 3568-3572.
7. Hou Z, Niu T, Zhao X, Liu Y, Yang T (2019) Intermetallic compounds formation and joints properties of electroplated Sn–Zn solder bumps with Cu substrates. J Mater Sci Mater Electron 30(22): 20276-20284.
8. Ramli M, Mohd SM, Yasuda H, Chaiprapa J, Nogita K (2020) The effect of Bi on the microstructure, electrical, wettability and mechanical properties of Sn-0.7Cu-0.05Ni alloys for high strength soldering. Mater Des 186.
9. George E, Pecht M (2016) RoHS compliance in safety and reliability critical electronics. Microelectron Reliab 65: 1-7.
10. Cheng S, Huang C, Pecht M (2017) A review of lead-free solders for electronics applications. Microelectron Reliab 75: 77-95.
11. Thomson J, Zavadil R, Sahoo M, Dadouche A, Dmochowski W, et al. (2010) Development of a Lead-Free Bearing Material for Aerospace Applications. Int J Met 4(1): 19-30.
12. Zhao X, Lai R, Hai X (2019) A Study on the Microstructures and Properties of Selective Laser Melted Babbitt Metals. J Mater Eng Perform 28(9): 5433-5440.
13. Dong B, Jie J, Dong Z, Chen Y, Zhong N, et al. (2019) Novel insight into mechanism of secondary phase's morphology evolution in hypomonotectic Cu-Pb-Sn alloy during solidification. J Mol Liq 292.
14. Dias M, Costa T, Soares T, Silva B, Cheung N, et al. (2017) Tailoring morphology and size of microstructure and tensile properties of Sn-5.5 wt.%Sb-1 wt.% (Cu,Ag) solder alloys. J Electron Mater 47(2): 1647-1657.
15. Taha M, El Mahallawy N, Hammouda R, Moussa T, Gheith M (2012) Machinability characteristics of lead free-silicon brass alloys as correlated with microstructure and mechanical properties. Ain Shams Eng J 3(4): 383-392.
16. Crepeau P (1995) Effect of iron in Al-Si casting alloys: A critical review. Trans Am Foundryman's Soc 103: 361-366.
17. Salguero J, Del SI, Gomez PA, Batista M (2020) Machining of Al-Cu and Al-Zn Alloys for Aeronautical Components. Intech Open 6.
18. Costa T, Dias M, Silva C, Freitas E, Silva A, et al. (2019) Measurement and interrelation of length scale of dendritic microstructures, tensile properties, and machinability of Al-9 wt% Si-(1 wt% Bi) alloys. Int J Adv Manuf Technol 105: 1391-1410.
19. Silva C, Leal L, Guimarães E, Júnior P, Moreira A, et al. (2018) Influence of Thermal Parameters, Microstructure, and Morphology of Si on Machinability of an Al-7.0 wt.% Si Alloy Directionally Solidified. Adv Mater Sci Eng.
20. Nascimento J, Barros R, Konno C, Silva A, Rocha O, et al. (2019) Machinability analysis of an Al-1,2% Pb alloy solidified in a horizontal directional device. Period Tche Quim 16(31): 860-874.
21. Silva A, Prado I, Barros J, Silva C, Moreira A, et al. (2015) Analysis of the cutting temperatures along the macrostructure of a directionally solidified Al-7wt%Si alloy. Defect Diffus Forum 365: 116-121.
22. Zhang P, Liu Z, Du J, Su G, Zhang J, et al. (2020) Correlation between the microstructure and machinability in machining Al-(5–25) wt% Si alloys. 234(9): 1173-1184.
23. Zedan Y, Samuel A, Samuel F, Alkahtani S (2012) The Influence of Microstructure and Composition on the Machinability of Al-Si Alloys. In: 13th International Conference on Aluminum Alloys.
24. Nascimento J, Magno I, Barros A, Vasconcelos A, Souza F, et al. (2021) Macrostructural Analysis of an Al-10%Sn Alloy Solidified in a Water-Cooled Horizontal Directional Device. Science and Eng Mater: Concepts, Fundam E Apl 1(1): 80-89.
25. Azevedo H, Botelho T, Barbosa C, Sousa A, Costa T, et al. (2020) Study of Dry Wear Behavior and Resistance in Samples of a Horizontally Solidified and T6/Heat-Treated Automotive AlSiMg Alloy. Tribol Lett 68(2): 1-17.
26. Magno I, Souza F, Costa M, Nascimento J, Silva A, et al. (2019) Interconnection between the solidification and precipitation hardening processes of an AlSiCu alloy. Materials Science and Technology 35(7): 791-806.
27. Rocha O, Costa T, Dias M, Garcia A (2018) Cellular/dendritic transition, dendritic growth and microhardness in directionally solidified monophasic Sn-2%Sb alloy. Trans Nonferrous Met Soc China 28(8): 1679-1686.
28. Oliveira R, Costa T, Dias M, Konno C, Cheung N, et al. (2020) Transition from high cooling rate cells to dendrites in directionally solidified Al-Sn-(Pb) alloys. Mater Today Commun 25.
29. Çadirli E, Böyük U, Engin S, Kaya H, Maraşli N, et al. (2009) Experimental investigation of the effect of solidification processing parameters on the rod spacings in the Sn–1.2 wt.% Cu alloy. J Alloys Compd 486(1-2): 199-206.
30. Machado A, Abraão A, Coelho R, Silva M (2015) Teoria Da Usinagem dos Materiais (3th ed.), Blucher, São Paulo.

31. Davies M, Ueda T, Saoubi RM, Mullany B, Cooke A (2007) On the Measurement of Temperature in Material Removal Processes. CIRP Ann 56(2): 581-604.

32. Santos M, Machado A, Barrozo M (2018) Temperature in Machining of Aluminum Alloys. Temperature Sensing.

33. Silva S, Filho J, Santos C, Costa T, Rocha O, et al. (2021) Machinability of an Al-6.0wt%Cu Alloy Solidified in a Horizontal Directional Device by Cutting Temperature Criterion. Brazilian J Dev 7(6): 60959-60971.

34. Trivedi R, Shen Y, Liu S (2003) Cellular-to-dendritic transition during the directional solidification of binary alloys. Metallurgical and Materials Transactions A 34(2): 395-401.

35. Trivedi R, Sekhar J, Seetharaman V (1989) Solidification microstructures near the limit of absolute stability. Metall Mater Trans A 20(4): 769-777.

36. Fu H, Geng X (2001) High rate directional solidification and its application in single crystal superalloys. Sci Technol Adv Mater 2(1): 197-204.

37. Abukhshim N, Mativenga P, Sheikh M (2006) Heat generation and temperature prediction in metal cutting: A review and implications for high speed machining. Int J Mach Tools Manuf 46(7-8): 782-800.

38. Engineering Tool Box (2003) Emissivity Coefficients common Products.

39. Dias M, Costa T, Rocha O, Spinelli J, Cheung N, et al. (2015) Interconnection of thermal parameters, microstructure and mechanical properties in directionally solidified Sn–Sb lead-free solder alloys. Mater Charact 106: 52-61.

40. O Sullivan D, Cotterell M (2001) Temperature measurement in single point turning. J Mater Process Technol 118(1-3): 301-308.

41. Alam M, Nai S, Gupta M (2009) Development of high strength Sn–Cu solder using copper particles at nanolength scale. J Alloys Compd 476(1–2): 199-206.

42. Chen S, Chen P, Wang C (2006) Lowering of Sn–Sb alloy melting points caused by substrate dissolution. J Electron Mater 35: 1982-1985.

43. Curtulo J, Dias M, Bertelli F, Silva B, Spinelli J, et al. (2019) The application of an analytical model to solve an inverse heat conduction problem: Transient solidification of a Sn-Sb peritectic solder alloy on distinct substrates. Journal of Manufacturing Processes 48: 164-173.

44. Mathew M, Yang H, Movva S, Murty K (2005) Creep deformation characteristics of tin and tin-based electronic solder alloys. Metall Mater Trans A 36(1): 99-105.